

An Absolute Flux Density Measurement of the Supernova Remnant Cassiopeia A at 32 GHz

Brian S. Mason^{1,2}, Erik M. Leitch^{3,4}, Steven T. Myers^{1,5}, John K. Cartwright³, and
A.C.S. Readhead³

ABSTRACT

We report 32 GHz absolute flux density measurements of the supernova remnant Cas A, with an accuracy of 2.5%. The measurements were made with the 1.5-meter telescope at the Owens Valley Radio Observatory. The antenna gain had been measured by NIST in May 1990 to be $0.505 \pm 0.007 \frac{\text{mK}}{\text{Jy}}$. Our observations of Cas A in May 1998 yield $S_{cas,1998} = 194 \pm 5$ Jy. We also report absolute flux density measurements of 3C48, 3C147, 3C286, Jupiter, Saturn and Mars.

Subject headings: standards — ISM: individual (Cassiopeia A) — planets and satellites: individual (Jupiter, Mars, Saturn) — quasars: individual (3C48, 3C147, 3C273, 3C286, 3C345) — galaxies: individual (3C84, 3C218, 3C353)

1. Introduction

Absolute flux density calibration is an important issue for all astronomical observations. Most absolute calibration efforts have occurred at lower frequencies ($\lesssim 10$ GHz) since it is easier to measure the far-field properties of antennas in this regime, or to use feed systems of calculable gain. See, for example, Conway et al. (1963), Kellermann (1964), Kellermann et al. (1969), Baars (1977) and references therein. Most of these flux density scales are

¹University of Pennsylvania, 209 S. 33rd St., Philadelphia, PA 19104-6396

²Current Address: California Institute of Technology, 105-24, Pasadena, CA 91125

³California Institute of Technology, 105-24, Pasadena, CA 91125

⁴Current Address: University of Chicago, 5640 S. Ellis Ave., Chicago, IL 60637

⁵Current Address: NRAO, Socorro, NM 87801

based upon measurements of the supernova remnant Cassiopeia A (Cas A) with horn-type or dipole antennas. At higher frequencies this endeavor is substantially more difficult, and investigators have often used flux densities extrapolated from low frequencies or computed from theoretical models of celestial sources. One exception is the work of Wrixon (1972), who measured the brightness temperature of Jupiter at frequencies between 20.5 and 33.5 GHz with a 20 foot antenna at the Hat Creek observatory; this telescope was calibrated with a far-field transmission/reception measurement. This measurement was the basis of the calibration used for the SZE measurements of Myers et al. (1998), but given the relatively large (5.5%) uncertainty in Wrixon's T_J it is desirable to improve upon this. This paper presents an *absolute* measurement with an accuracy of 2.5% of the flux density of Cas A at 32 GHz, a calibrator commonly used at all frequencies and the second brightest extrasolar source in the sky in our observing band.

While absolute calibration is an important consideration for many different types of experiments, our calibration efforts were undertaken with the particular intent of supporting the intrinsic CMB and Sunyaev-Zeldovich programs at the Owens Valley Radio Observatory (OVRO) and other similar observations. Absolute calibration is an especial concern for Sunyaev-Zeldovich studies since the error in the quantity of interest (H_o) is proportional to twice the calibration error. It is of great importance that the calibrations of intrinsic CMB anisotropy experiments be as accurate as possible in order to place more stringent limits on the parameters of cosmology. Several published CMB experiments use Cas A as their primary calibrator, such as the Saskatoon experiment (Netterfield et al., 1996) and CAT (Scott et al., 1996). These experiments typically have calibration uncertainties $\gtrsim 10\%$. It is important to reduce these uncertainties as much as possible and to use a single flux density scale at or near 32 GHz. This affects a number of experiments including the RING5M (Leitch et al., 1999), MAT (Torbet et al. 1999; Miller et al. 1999), QMAP (Devlin et al., 1998), CBI (Readhead et al., 1998), DASI (White et al., 1998) and the VSA (Jones and Scott, 1998).

The 1.5-m telescope used in the present observations was originally designed and constructed by JPL as part of the Deep Space Network (DSN) program. The telescope has a parabolic primary reflector with an off-axis secondary and a dual feed horn, and a Dicke-switching receiver at the Cassegrain focus. To establish absolute gain standards for DSN, the National Institute of Standards and Technology (NIST) was employed to measure the aperture efficiency of the 1.5-m antenna; these measurements are discussed in § 2. OVRO obtained the instrument in 1993, and our current calibration program commenced in 1996, with efforts focused on characterizing the receiver and reworking the telescope control code. Most of the useful astronomical observations were taken during the spring of 1998 (from early March through the end of May).

We selected Cassiopeia A ($\alpha = 23^{\text{h}}23^{\text{m}}26^{\text{s}}.920$, $\delta = +58^{\circ}49'07''.50$, J2000) as our primary calibration source because of its brightness and accessibility from the latitude of the observatory. Observations of other calibrator sources relative to Cas A were carried out in the fall of 1998, as well as during epochs previous to our absolute measurements, allowing the determination of absolute flux densities for these sources as well.

In the following, we first present a brief description of the NIST calibration measurements (§ 2) and our own characterization of the instrument (§ 3); following this is a summary of observations taken at OVRO in the spring of 1998 (§ 4), and a detailed discussion of our error budget (§ 5). Next we describe observations of 3C48, 3C147, 3C286, Jupiter, Mars, Saturn and other sources on the OVRO 5.5-meter telescope relative to Cas A, employing our absolute value for S_{cas} (§ 6). Finally we summarize our findings and compare them to the results of other flux density scales (§ 7).

2. Antenna Characterization: NIST Measurements

Flux density, S_{ν} , is related to the spectral power, P_{ν} , by

$$P_{\nu} = A_{eff}(\nu) \times S_{\nu}, \quad (1)$$

where $A_{eff}(\nu)$ is the *effective area* of the telescope. A_{eff} is always less than the geometrical area of the telescope for a well-designed system due to diffraction at the edge of the dish, surface irregularities, scattering off of the secondary support structure (not a problem for unblocked apertures such as this one), slight impedance mismatches, and so forth. The most difficult aspect of most absolute flux density measurements at high frequency is the accurate assessment of A_{eff} .

It can be shown from elementary thermodynamic considerations (e.g., Rohlfs and Wilson, 1996; Krauss, 1986) that

$$\Omega_{Ant} \times A_{eff} = \lambda^2 \quad (2)$$

where λ is the wavelength of the incident radiation and

$$\Omega_{Ant} = \iint d\phi d(\cos\theta) P_{Ant}(\theta, \phi). \quad (3)$$

Here $P_{Ant}(\theta, \phi)$ is the response function of the antenna normalized to one at the maximum. If we define the *gain*, g , of a telescope in a given direction as the ratio of P_{Ant} in that direction to the mean value of P_{Ant} on the sphere, then it can be shown that

$$g|_{max} = \frac{4\pi}{\Omega_{Ant}}. \quad (4)$$

Since g is a ratio, it is often expressed in decibels (dBi, or decibels above the isotropic level implied by the spherical average).

It is convenient to express spectral power in terms of the *antenna temperature* T_{Ant} , defined as the temperature a beam-filling blackbody would need to have (in the Rayleigh-Jeans limit) in order to produce the observed spectral power. The antenna system may then be characterized by the Kelvin per Jansky *sensitivity*, Γ :

$$\Gamma = \frac{\lambda^2}{8\pi k} \times g|_{max}. \quad (5)$$

Numerically, this is

$$\Gamma = 0.362 \times \frac{A_{eff} \text{ mK}}{\text{meters}^2 \text{ Jy}}. \quad (6)$$

In the far-field of a given antenna, these properties (Γ , A_{eff} , Ω_{Ant}) are independent of distance. The far-field is conventionally defined to be the distance at which the phase variation (across the aperture of the antenna) of an electric field originating at a point at distance r_{ff} is less than 22.5° ; this criterion yields a beam pattern which is, to a good approximation, independent of the distance of the illuminating source from the antenna. For a flat aperture the given phase constraint results in $r_{ff} > 2D^2/\lambda$.

Since for many telescopes the far-field is inconveniently far away, the direct measurement of far-field antenna characteristics often requires measurements to be made over long distances outside of a controlled laboratory setting. In this context, boresighting, ground reflections and atmospheric attenuation are all difficult issues to deal with. Extensive work has consequently been done at NIST and elsewhere to develop near-field techniques to measure the far-field power pattern and gain of antennas; this work and the theory behind it is summarized in Baird et al. (1988) Lo and Lee (1993) Newell et al. (1988) Rahmat-Samii (1993). The technique employs a measurement of the near-field electric field of the antenna; the resulting field distribution (after correcting for the probe antenna characteristics) is related to the far-field electric field by a Fourier transform. Ranged measurements are used to fit out mutual coupling terms due to imperfect impedance matching between the target and probe antennas (Lo and Lee, 1993 ; Francis, 1990); the probe gains themselves are determined using a three-antenna technique (Lo and Lee, 1993). In May of 1990, our telescope was characterized at NIST’s near field test range in Boulder, Colorado (NIST, 1990). The compactness of the antenna permitted this procedure to be carried out without disassembling the instrument for shipping, greatly reducing uncertainties which may otherwise arise due to the relative displacement of the various optical components of the system; for more discussion of this point, see § 5. NIST assigns a 1.4% ($1 - \sigma$) systematic error to this measurement in the calibration report; this uncertainty is dominated by the determination of the probe antenna gain and normalization amplitude. As discussed in § 3,

ν (GHz)	g (dBi)	g (10^5)	A_{eff} (m^2)	η_A	G (mK/Jy)
31.8 (ANT)	52.54 ± 0.06	1.795	1.270	71.9%	0.460 ± 0.006
32.0 (ANT)	53.04 ± 0.06	2.014	1.407	79.6%	0.509 ± 0.007
32.0 (REF)	52.96 ± 0.06	1.977	1.381	78.1%	0.500 ± 0.007
32.3 (ANT)	53.32 ± 0.06	2.148	1.472	83.3%	0.533 ± 0.007

Table 1: NIST antenna gain measurements

the 1.5-meter is outfitted with a Dicke-switching receiver with two horns. The gains of these horns were separately measured; we designate them the ANT and REF horns. The NIST gains, however, are referred to the *back* of the feed horns. This implies that the stated gains include the effects of ohmic losses in the feeds, whereas our calibration procedure effectively removes these losses. We will account for this in our final systematic error budget.

The ANT beam gain was measured at 31.8, 32.0 and 32.3 GHz ; the REF beam gain was only measured at 32.0 GHz. These measurements are summarized in Table 1. Note that the measured gains at the band edges differ by 13.6%; while the nominal receiver bandpass is 3 GHz, it is clear that the extrapolation of the observed gains to 30.5 and 33.5 GHz will introduce a very large uncertainty. Furthermore, the REF beam was only characterized at the band center. For these reasons an additional filter was introduced into the signal path, reducing our system bandpass to 500 MHz centered on 32.0 GHz (see § 3). We therefore adopt the mean of the ANT and REF beam gains at 32.0 GHz, $g = (1.995 \pm 0.028) \times 10^5$ (53.00 \pm 0.06 dBi), corresponding to $\Omega_{Ant} = (6.298 \pm 0.088) \times 10^{-5}$ Sr, $A_{eff} = (1.394 \pm 0.020)$ meters² and $\Gamma = (0.505 \pm 0.007) \frac{mK}{Jy}$. Assuming a geometrical area of 1.77 meters², this yields an aperture efficiency of (78.8 \pm 1.1)%. The average of the ANT and REF gains is the appropriate quantity to use in the context of our double-differenced FLUX procedure (see § 4).

NIST also measured the beam patterns of both ANT and REF beams; the beams were found to be well-described by Gaussians of $25'.8 \pm 0'.6$ FWHM, corresponding to $\sigma = 10'.96 \pm 0'.25$. Integrating a Gaussian of this width out to the radius of the first measured nulls in the beam pattern (at $\pm 24'.0$), we compute $\Omega_{Beam} = (5.80 \pm 0.26) \times 10^{-5}$ Sr and a beam efficiency of

$$\begin{aligned} \eta_{Beam} &= \frac{\Omega_{main}}{\Omega_{Ant}} \\ &= 87.0 \pm 4.8\%. \end{aligned}$$

The beam throw was measured to be $1^\circ.00 \pm 0^\circ.01$, with a $0^\circ.02 \pm 0^\circ.1$ ($= EL_{ANT} - EL_{REF}$)

elevation offset. The relatively high beam and aperture efficiencies demonstrate the efficacy of the clear-aperture design and small, stiff primary dish.

It is likely that the 1.8% difference between the ANT and the REF gains is due to a slight impedance mismatch on the REF side of the signal chain; NIST measured the return loss on the REF horn to be several dB lower than that on the ANT horn. This could be due to differential isolation in the Dicke switch.

3. Receiver Characterization and Antenna Temperature Calibration

The receiver is a standard Dicke-switching two-horn receiver. Celestial signals enter the receiver via these two scalar feeds (uncooled) and pass into the 15 K dewar where right circular polarization is selected. A cross-guide coupler before the Dicke-switch permits the injection of a calibration (cal) signal. The Dicke-switch itself operated at 1 kHz during observations, providing alternating 0.5 msec “integrations” against each feed. The switched signal is amplified by a HEMT (+28 dB of gain), the last component in the 15 K dewar. The 15 K cryogenic stage displayed remarkable stability from fall 1996 through spring 1998.

The 15 K dewar is enclosed in a dewar which is maintained at ~ 70 K. On entering this stage, the RF passes first through an Avantek amplifier (second stage, +22 dB) and then through a double-sideband mixer, which converts the signal down to a 0 to 1.5 GHz IF. Before leaving the dewar, the IF is amplified and passed through a 1.5 GHz low-pass filter. This signal is piped via coaxial cable to a climate-controlled trailer where the detection and post-detection signal processing is carried out. For the reasons detailed in § 2, detection of the full band power is undesirable, so this signal was passed through a 250 MHz low-pass filter, giving a system bandpass of 500 MHz on the sky; the resulting signal is split, half going to a diode detector, which feeds a Lock-in-Amplifier (LIA) for the detection of switched power, and half going to an HP 437B power meter for detection of total power. In order to boost the IF signal well above the lowest levels that the LIA was capable of detecting, another IF amplifier (+17 dB of gain) was inserted in the signal chain after the coaxial cable and before the final low-pass filter.

The linearities of the power meter power head and diode detector were assessed by measuring the cal signal increment with an ambient-temperature microwave absorber placed in front of the feed-horns and varying the attenuation prior to the powerhead and detector. The diode detector’s departures from linearity over the dynamic range encountered in calibration observations is less than 0.1%; the power head’s deviation is less than 0.2%. These elements are thus not significant sources of nonlinearity. The receiver on the other

hand is somewhat nonlinear, which is discussed below.

The Dicke switch isolation was measured by locking the switch onto the ANT feed while repeatedly firing the cal signal into the REF feed. In 112 pairs of on/off averages of the system power, a mean fractional increase in the system temperature of $(5.7 \pm 1.3) \times 10^{-4}$ was observed. These tests were conducted against an external cold load for stability; assuming $T_{RX} = 55 \text{ K} + 77 \text{ K} = 132 \text{ K}$ and $T_{cal} = 14.34 \text{ K}$ (see below), this implies a leakage of $0.54 \pm 0.11\%$ of the cal signal. This is equivalent to an isolation of $-22.7 \pm 0.9 \text{ dB}$. Any effects such as losses or a finite duty cycle in the Dicke switch do not affect our results as they will affect celestial observations and observations of our calibration loads in the same fashion (see below).

Although the receiver design incorporates several mechanical waveguide switches which permit some degree of control over the magnitude of the cal diode signal, these switches were not exercised *at any point* during or between our calibration measurements and observations. This precaution was deemed necessary due to the possibility that the switches might not toggle between two precisely defined impedance states, which would cause the apparent cal signal brightness to change. The receiver does not have any variable attenuators, which would have to be calibrated at a number of settings.

Although the NIST calibration allows the accurate computation of flux densities given T_{Ant} , the task of determining T_{Ant} from observed quantities (milliVolts) is not trivial. This issue is more important in the context of an absolute measurement, since for experiments which use an external flux density reference the sensitivity (K/Jy) and the receiver gain (mV/K) are not determined independently: the overall gain (mV/Jy, or some equivalent quantity) is obtained directly. Consequently, great care was taken in designing a power (T_{Ant}) calibration scheme. This task is made somewhat easier by the fact that we measure the antenna temperature in units of the cal signal, whose derived magnitude is not highly sensitive to slight errors in our brightness temperature references (two microwave absorbers at known thermodynamic temperatures— see § 5, and below).

To measure the receiver temperature T_{RX} of our system and the effective brightness temperature T_{cal} of our cal signal, we use the standard hot-cold load scheme. Our hot load is an ambient temperature microwave absorber and our cold load is an absorber immersed in liquid nitrogen. The increment in total power is measured against each of these loads providing a measurement of T_{cal} , T_{RX} and the receiver nonlinearity. The loads themselves are our ultimate temperature references. In terms of the temperatures of the hot and cold loads, the receiver temperature T_{RX} is given by

$$T_{RX} = \frac{T_{hot} - yT_{cold}}{y - 1} \quad (7)$$

where y is the observed ratio of total power against the hot load to total power against the cold load. Once T_{RX} is known, the effective brightness temperature of the cal diode may be determined by observing the total power against either of the hot or cold loads with the cal diode on and off. For observations against the cold load, we find

$$T_{cal} = \frac{y_{cal} - 1}{y - 1} (T_{hot} - T_{cold}) \quad (8)$$

where y_{cal} is the ratio of the total power observed with the cal diode on to total power observed with the cal diode off. If T_{cal} is derived from observations against the hot load, we find

$$T_{cal} = \frac{y_{cal} - 1}{y - 1} y (T_{hot} - T_{cold}). \quad (9)$$

Since observations at lower power levels are less affected by increased system noise and nonlinearity (see below), we derive T_{cal} from observations against the cold load.

The microwave absorber employed for each load was a 3-inch thick sheet of ECCOSORB CV⁶. Tests at liquid nitrogen temperature indicate that the absorber had an optical depth $\tau > 7.4$. At ambient temperatures, the optical depth is expected to be higher (Hemmati, 1985), but this measurement is more difficult due to the increased system noise. The cold load was assumed to have a thermodynamic temperature equal to the boiling point of liquid nitrogen (76.3 K at atmospheric pressures characteristic of the Owens Valley). The front-face temperature of the hot load was measured with a hand-held infrared thermometer; this thermometer was calibrated (using ECCOSORB-CV) against a platinum resistance thermometer with a specified accuracy at room temperature of ± 0.02 K. While in principle this calibration may have been necessary to relate the thermodynamic temperature to the effective infrared brightness temperature over the IR thermometer’s bandpass (i.e., to correct for the unknown and presumably finite IR emissivity of ECCOSORB-CV) we found that both thermometers measured the same temperatures to ~ 0.1 K. Assuming that $\tau \geq 7.4$ for our absorber, the thermodynamic and brightness temperatures for both loads are identical to better than 0.1%. Given our measured optical depth, temperature gradients across the hot load do not significantly affect our measurements provided we measure the temperature of the front face of the absorber.

The manufacturer’s specifications indicate that reflections from the absorber at 32 GHz are suppressed by 50 dB. The cold load cooler is constructed of a cross-linked polyethylene foam, which possesses good thermal properties and has a very low optical depth at microwave frequencies ($\tau \sim 7 \times 10^{-3}$). Laboratory measurements of the cooler

⁶ECCOSORB is a registered trademark of Emerson and Cuming Microwave Products.

show that it evinces a brightness temperature ~ 0.7 K higher than a cone of absorber dipped in liquid nitrogen. This measured brightness temperature excess is also consistent with the expected brightness temperature of a 300 K emitter with an optical depth of $\tau = 7 \times 10^{-3}$. We correct the cold load brightness temperature for this emission. In spite of the simplicity of the cone-load arrangement, these loads were not used for daily T_{RX} and T_{cal} measurements due to their lack of long-term emission stability. One potential concern which arises in the usage of a liquid-nitrogen-filled cooler is the impedance mismatch at the box-nitrogen interface; if there is significant power being emitted out of the horns (presumably of order T_{RX}), then some fraction of this power would be reflected back into the system, artificially increasing the measured receiver temperature. To the end of calibrating the first OVRO SZE experiment, Herbig et al. (1994) constructed a cold load box of the same cross-linked polyethelyene foam with an impedance-matching network on one side. This network consisted of a hexagonal pattern of (liquid-nitrogen-filled) holes on the inside of the cooler wall which provides a refractive index intermediate to that between free space and liquid nitrogen. No significant difference in power was observed between the matched and unmatched sides of the cold load. This together with the good agreement between the measured and theoretically computed box emission, show that neither internal reflections nor other excess emission mechanisms contribute significantly to our cold load measurement. For a more detailed discussion on the effects of excess emission on our T_{ant} calibration, see § 5.

In the taking of T_{RX} measurements, a $\sim 5\%$ receiver nonlinearity is seen (a compression of the cal signal at the hot load total power levels relative to what is seen at cold load power levels). Most likely this is due to a slight compression of the second or third stage amplifiers. We correct our measurements for nonlinearity by assuming that our system response P_{obs} to an input power P_{true} is described by

$$P_{obs} = g \times (1 + bP_{obs}) \times P_{true}, \quad (10)$$

where g is the receiver gain and b characterizes the nonlinearity in the system. For small excursions from perfect linearity as observed this should be a good description. This is the same description employed by Leitch et al. (1999) with good results on the OVRO 5.5-m Ka-band system, as well as the 40-m Ku-band system.

We measure b on an observation-by-observation basis by equating the cal signal increments observed against the hot and cold loads and solving for b . It is not significant to quote a mean value for b since this depends on g at the time of the observation which is significantly time variable. Application of this correction to each data point reduced the mean T_{cal} by 2%, and T_{RX} by 8%.

To measure the effectiveness of a nonlinearity correction based on Eq. 10, it is

convenient to compare the cal diode increments observed against hot and cold loads to the increment observed against the sky at zenith. For all the data taken in the 14 T_{cal} measurements, prior to the application of the nonlinearity correction the ratios of the raw cal increment observed against the hot load to the raw cal increment observed at zenith, and the equivalent quantity for the cold load, are 0.95 ± 0.01 and 0.99 ± 0.01 respectively. After the application of a nonlinearity correction derived separately for each observation, this ratio (for both loads) is 1.00 ± 0.02 . Since no information about the cal signal increment at zenith was employed in the derivation of b , this is an independent indication that our simple model is a good description of the system non-linearity over the whole range of powers relevant to our observations.

Using this arrangement we measured T_{RX} and T_{cal} on 14 separate occasions during the period 10 May 1998 through 15 May 1998; after correcting for receiver nonlinearity and the Dicke-switch isolation, as well as applying a slight correction⁷ for deviations from the Rayleigh-Jeans law, we find $T_{RX} = 54.8 \pm 0.9$ K and $T_{cal} = 14.34 \pm 0.07$ K (measurement error only).

4. Observations

The radiometry procedures used in observations on the 1.5-m telescope are the same as those used on the other single-dish radio telescopes at OVRO. The two fundamental procedures are FLUX and CAL measurements. A FLUX measurement is a double switched measurement in which the source is alternately placed in the REF and ANT beams; two integrations of switched power are executed in each position. This cancels out constant and linear power backgrounds in the measurement, such as those caused by the atmosphere, receiver noise and ground pickup. A CAL procedure consists of two integrations of switched power with the cal diode signal being injected into one of the receiver arms, bracketed by two integrations of switched power with the cal signal off. For more detail on these procedures refer to Readhead et al. (1989), Myers et al. (1997), and Leitch et al. (1999). It is additionally possible to record (singly) switched power; this procedure is known as an AVERAGE. By doing a set of AVERAGEs around the nominal pointing center of some source, it is possible to derive the pointing offsets; this is known as a POINT procedure. Generally four AVERAGEs were done spaced at $\pm 0^\circ.27$ in azimuth and elevation around the source.

⁷This correction amounted to a 0.4% adjustment of our measured hot load temperatures, and a 0.8% adjustment of our assumed cold load temperature.

In March 1998 two days of pointing data were taken on bright celestial sources (Cas A, the Crab and Venus). These observations consisted of a cycle of POINT, FLUX, and CAL procedures executed repeatedly against the source in long tracks. From these data a pointing model was derived which reduced the rms pointing offset from 15'.4 to 2'.2 (0'.85 on Cas A) in addition to removing overall systematic pointing offsets. This is the pointing model which was used in subsequent observations. Due to the weather conditions in May reliable pointing tests were not possible, but for a small stiff dish such as this that presents no problem, as all of the pointing errors are likely to be constant offsets.

On 22 April 1998, observations of Cas A consisting of alternate pointings on the ANT and REF beam positions were taken in order to confirm the NIST-measured beamthrow. We found, relative to these fixed offsets, an azimuth separation of $0'.04 \pm 0'.12$, and a zenith angle separation of $0'.70 \pm 0'.26$. We take this to be consistent with the nominal $(\Delta AZ, \Delta EL) = (-1^\circ.0 \pm 0^\circ.01, 0^\circ.0 \pm 0^\circ.1)$ offsets. Given our 25'.8 FWHM main beam, the neglect of the 0'.7 ANT/REF zenith angle offset amounts to a potential 0.3% systematic error in our FLUX measurements.

During the period 10 May 1998 – 16 May 1998, observations of Cas A were conducted when the weather permitted. These observations consisted of FLUXes (10 second integrations in each segment, with 15 second idle times to allow the telescope to acquire the position) interleaved at 10 minute intervals with CAL's (10 second integrations, 5 second idles). The pointing model described above was employed. Full tracks on the source were used in order to average out variations in atmospheric opacity or residual ground spillover over the course of a track.

The data were calibrated by scaling the observed FLUXes by the ratio of observed CAL's to the measured cal diode temperature ($T_{cal} = 14.34 \pm 0.07$ K). Since the CAL and FLUX measurements were taken at the the same power level no nonlinearity correction is necessary. If the standard deviation of any individual CAL or FLUX procedure is more than four times the average standard deviation observed in the entire data set, that datum is rejected. Similar $5 - \sigma$ edits were performed on the CAL and FLUX means. These edits remove a negligible fraction of the data but eliminate grossly discrepant data points caused by atmospheric interference or rare instrumental glitches.

Since the atmosphere has a significant opacity to microwave radiation, it is necessary to apply a correction for atmospheric attenuation. The observed flux density of a source as a function of zenith angle is

$$S(ZA) = S_o e^{-\tau \sec(ZA)}, \quad (11)$$

at 32 GHz, the optical depth τ is typically less than 0.1 when observations are conducted. Opacity corrections were determined by a straight-line fit of the natural logarithm source

flux densities to $\sec(ZA)$, and the data multiplied by $e^{+\tau \sec(ZA)}$. Data at $ZA > 70^\circ$ were excluded from the analysis. The 10 May 1998-16 May 1998 data set as a whole has a mean optical depth $\tau = 0.071$. Figure 1 shows the raw FLUX data uncalibrated for atmospheric attenuation. The straight-line fit in this figure corresponds to $\tau = 0.071$.

The weighted mean of the calibrated data yields $S_{cas} = 194.0 \pm 0.4$ Jy (measurement error only). The fully calibrated data are plotted versus ZA in Figure 2. The solid line shows the mean for all of the FLUXes, and the dashed lines show our $1 - \sigma$ error bars (see § 5). For clarity, the data have been binned into 100 equal bins in ZA . These data show evidence for some contamination at the ~ 3 Jy level; this is likely due to ground spillover which was not entirely eliminated by our double-differencing. An effect of similar magnitude is seen in the data plotted against parallactic angle (Fig. 3). Exclusion of the data at $ZA > 50^\circ$ (data of notably lower quality) leaves the mean unaffected to $< 0.02\%$. The overall gradient in the FLUXes as a function of parallactic angle is well-correlated with ambient temperature and we therefore suspect that it is due to imperfect temperature control of the cal diode; this was confirmed in calibration observations taken in October and December of 1998. Since the T_{cal} measurements themselves were taken at a wide range of ambient temperatures, this is not likely to bias our result. The fact that the the FLUXes as a function of ZA are roughly consistent with a constant value ($\chi^2_\nu = 1.62$ for 89 degrees of freedom) is an indication that the parallactic angle variations average out over the course of a track. In any case both of these effects are well within our calculated $1 - \sigma$ systematic error limits, which we describe in the next section.

5. Systematic Error Budget

In this section we present our estimate of the contributions of various systematic effects to our measurement. We consider these effects in order of their importance.

The dominant source of uncertainty for our measurement is the NIST gain measurement error (1.4%). Short of recalibrating the telescope, there is little that can be done to reduce this. Due to the differing reference planes of the NIST gain measurement and our hot/cold load calibration (see § 2), there is an additional uncertainty which we estimate to be about 1% due to ohmic losses in the feeds. This would have the effect of making the NIST gain artificially low, hence affects our inferred flux density only in the negative direction.

Based on the rms of the fluxes derived from individual days' observations we estimate that τ contributes no more than a 1.0% potential error to our measurement.

Since the observed ground spillover and T_{cal} effects noted in § 4 will average out to some

extent over a track (and as T_{cal} measurements are taken at different ambient temperatures), we take these to contribute independent systematic errors at the level of half the observed maximum departure from the mean. Since the observed fluctuations are ~ 3 Jy in each case, this results in two contributions of 0.8% to our systematic error budget.

Since Cas A is located very close to the Galactic Plane ($l = 111^\circ.74, b = -2^\circ.128$), there is the possibility that our measurements are contaminated by foreground sources, such as bright HII regions associated with young stellar systems, as well as by flat spectrum background radio galaxies present at all galactic latitudes. Unfortunately Cas A is the second brightest extrasolar source in the sky at our observing frequency, with the consequence that radio surveys of this region of the sky tend to be heavily contaminated due to the telescope sidelobes; on the other hand, the high overall flux density of Cas A reduces the fractional significance of interloping sources. The primary concern for observations with our dual-feed system is that a contaminating point source may pass through the scan pattern of one of the reference beams. Since the reference beams move on the sky relative to the nominal pointing center (Cas A), such an event introduces a characteristic Hour Angle dependence into our data. Based on the data that we have collected, we place an upper limit of 16 Jy on the magnitude of possible point source contamination in the reference beams. We should indicate that while some of the individual features in Figure 3 are consistent with the signature of a single point source, all of them *jointly* are not. In particular, the feature centered at $PA = -20^\circ$ is consistent with a contaminating point source of about 16 Jy, but the double feature (including the feature centered at $PA = 33^\circ$) is *not* well represented by two point sources. We conclude therefore that most of the signal observed is residual ground spillover. Using a model which realistically accounts for the motion of the reference beams during a scan, a 16 Jy source placed at the *center* of one of our reference beams would bias the average flux density we infer for Cas A by 1.08 Jy (0.6%). We adopt this as a $1 - \sigma$ upper limit on possible point source confusion. Since there are only a handful of sources in the whole sky at 32 GHz with flux densities greater than a few Jy, this is likely to overestimate the level of point source contamination.

The accuracy of our pointing algorithm was determined using a Monte-Carlo simulation with realistic signal-to-noise statistics. The pointing error is dominated by the model residuals, which could be improved by more pointing in good weather. The overall pointing error is estimated to contribute a 0.7% systematic error to our result, of which 0.5% comes from the pointing model residuals.

While determining the cal diode brightness temperature, T_{cal} , is one of the most crucial aspects of our experiment, we have been able to do so very precisely, so this error is one of the least significant contributors to our error budget. This is largely due to the fact that

T_{cal} is relatively insensitive to errors in the load temperatures. Using Equation 8, which takes into account the implicit load-temperature dependence of our system temperature determination, we find that the error in T_{cal} induced by an error in the expected cold load temperature T_{cold} is

$$\epsilon(T_{cal}) = -\frac{y_{cal} - 1}{y - 1} \times \epsilon(T_{cold}) \quad (12)$$

and the corresponding error due to the hot load is

$$\epsilon(T_{cal}) = \frac{y_{cal} - 1}{y - 1} \times \epsilon(T_{hot}) \quad (13)$$

With the observed values of $y \sim 2.71$ and $y_{cal} \sim 1.11$, this yields about 0.6% of error in T_{cal} per degree K of error in either of the hot or cold loads. Adopting $\epsilon(T_{hot}) = 0.5$ K and $\epsilon(T_{cold}) = 0.7$ K and adding these errors in quadrature, we obtain a 0.5% error in T_{cal} .

Even though there is a fairly significant nonlinearity in our receiver system, it affects our T_{ant} calibration at only the 2% level and so even relatively larger errors in the characterization of the nonlinearity affect us at $\lesssim 0.4\%$ level. Systematic errors in T_{hot} or T_{cold} do not significantly affect this characterization since the nonlinearity measurements depend only on the observed cal signal *increment* against each of these loads.

In general the gain and source spectrum may vary across the band, and this may be a significant source of error for observations with a wide bandpass. For a source with a flux density $S(\nu)$ observed on a system with a frequency-dependent effective area $A_{eff}(\nu)$, the band-averaged spectral power is

$$\overline{P_{obs}} = \frac{1}{\Delta\nu} \int_{\nu_o - \Delta\nu/2}^{\nu_o + \Delta\nu/2} d\nu S(\nu) A_{eff}(\nu), \quad (14)$$

where ν_o is the band center and $\Delta\nu$ the total bandpass. If both $A_{eff}(\nu)$ and $S(\nu)$ can be reasonably approximated as power laws over this interval, then the band-averaged spectral power can be shown to be

$$\overline{P_{obs}} = A(\nu_o) \times S(\nu_o) + O\left(\frac{\Delta\nu}{\nu_o}\right)^2. \quad (15)$$

Variations in these quantities thus induce errors proportional to the fractional bandpass $\Delta\nu/\nu_o$ squared in the flux densities and brightness temperatures one infers under the assumption that one is measuring $S_\nu(\nu_o)$ instead of the band averaged flux density. For our narrow (2%) bandpass, this introduces errors at less than the 0.1% level and may be safely neglected.

Another potential concern for very accurate measurements made with dual-feed systems is that the sidelobes of one beam will be present at a significant level in the other

beam, reducing the average gain of a doubly-switched measurement. Since the secondary is illuminated asymmetrically, the sidelobes of one beam in the direction of the other tend to be highly suppressed. The NIST measurements indicate that the sidelobes of one beam are suppressed by $\gtrsim 35$ dB near the maximum of the other beam (NIST, 1990); in contrast, the nearest sidelobes on the other side are at -20 dB. This is therefore not a concern for our system.

Our systematic error budget is summarized in Table 2. Adopting our measured value of $S_{cas} = 194.0 \pm 0.4$ Jy and the above calculation of our systematic error we have $S_{cas,1998} = 194 \pm 5$ Jy at 32.0 GHz.

Source	Sense	Fractional Magnitude
Nonlinearity	\pm	0.2%
T_{cal} (systematic)	\pm	0.5%
T_{cal} (meas.)	\pm	0.5%
Point Source Confusion	+	0.6%
Pointing	+	0.7%
Unsubtracted Ground Spillover	\pm	0.8%
T_{cal} Variations	\pm	0.8%
Atmospheric Opacity	\pm	1.0%
Ohmic Losses in Feeds	–	1.0%
Antenna Calibration	\pm	1.4%
Total		$\pm 2.4\%$

Table 2: Total Systematic Error Budget for 1.5-m Absolute Flux Measurement of Cas A

6. 5.5-meter Observations and Leveraged Flux Density Scale

While Cas A is a useful calibrator for experiments with very large beams ($\theta_{FWHM} \gtrsim \theta_{casA} \sim 5'$), it is not so useful for instruments with smaller beams, or for experiments at southern latitudes. It is therefore desirable to apply our absolute flux density measurement to a set of calibrators of smaller angular extent at a wide range of declinations. To this end, we have analyzed five epochs of observations of a set of calibrators (the choice of which is discussed below) relative to contemporaneous observations of Cas A. These observations were taken with the OVRO 5.5-meter telescope outfitted with a 32-GHz Dicke-switching receiver system with a ~ 6 GHz bandpass at 32 GHz. The primary beam of this instrument has two beams with a FWHM of $7'.35$ and a separation of $22'.17$. Using these observations plus our absolute value for S_{cas} we can establish an absolute flux density scale at our observing frequency for the set of sources we observed.

The epochs of observation were chosen from archival OVRO data with the criteria that the source observations consist of observations of any of our sources close to observations of Cas A, that the observations occur over a reasonably wide range of Hour Angles and that the observing conditions be sufficient to obtain a reasonable signal-to-noise on the source(s) over the observation as a whole. The data we selected fall into five epochs from December 1994 to October 1998; these epochs, together with the serial number of the HEMT present in the receiver at the time of the observations (see discussion below) are shown in Table 3.

Our choice of sources was dictated by the requirement that the calibrators be bright, relatively small in angular extent, and (for the most part) non-variable. The sources we chose are NGC7027, 3C48, 3C84, 3C84, 3C147, 3C218, 3C273, 3C286, 3C345, 3C353, Jupiter, Saturn and Mars. The sources 3C48, 3C147 and 3C286 are quasars with steep spectra, and are regularly observed at the VLA as primary flux calibrators. The latter

Epoch	Dates	HEMT ID
1	21dec94 – 23dec94	NRAO A-12
2	03feb95 – 07feb95	NRAO A-12
3	20apr95 – 05may95	NRAO A-12
4	29nov97 – 09dec97	NRAO A-23
5	22oct98 – 28oct98	MAO-5

Table 3: Epoch definitions for source observations reported in this section, along with the HEMT in place in our receiver during the observations. See Table 4 for the receiver band characteristics for each HEMT.

sources, and in particular Jupiter and Mars, are frequently used calibrators at centimeter wavelengths. The possible variability of some of these sources will be discussed below.

Since Cas A is comparable in size to the 5.5-meter primary beam, it is necessary to correct the observed flux densities for the effect of the convolution of the sky brightness with the telescope beam pattern. The details of this procedure are discussed by Leitch et al. (1999) and Leitch (1998). In brief, a high-resolution map of Cas A made at 32 GHz on the Effelsberg telescope (Morsi 1997) was used as a brightness template in a Monte Carlo simulation, incorporating uncertainties in the 5.5-meter beam pattern and pointing model, to determine the ratio f of the total flux density of Cas A to the flux density observed with the 5.5-meter on Cas A. The 68% confidence interval of the resulting distribution is $f = 1.18_{-0.01}^{+0.02}$. This is the factor by which the 5.5-meter observed S_{cas} values must be multiplied to obtain the total flux density of Cas A, as would be observed by a telescope with a primary beam much larger than the extent of Cas A itself. This allows us to relate the 5.5-meter observations of alternate calibrator sources *relative* to Cas A to our *absolute* measurement of Cas A with the 1.5-meter telescope.

Given the wide bandpass of the 5.5-meter receiver system the variation of the source spectra across the observed band and the bandpass of the observing band itself must be accounted for. Leitch (1998) has extensively characterized the band properties of the 5.5-meter receiver from 1994 - 1997. Over this time period, two different HEMT's were employed in the receiver, and the receiver in each of these states has been fully characterized separately. In May of 1998, A-23 suffered a catastrophic failure and was replaced with the MAP non-flight HEMT MAO5. A full characterization of the receiver with MAO5 in place has not been undertaken, but the data we have in hand are in reasonable agreement with the bandpass of A23. From these, we estimate $\delta\nu = (6.6 \pm 0.6)$ GHz, $\nu_{cent} = (31.9 \pm 0.3)$ GHz for the receiver with MAO5. Our adopted band characterizations are summarized in Table 4.

The strategy we choose is to interpolate the broadband 5.5-meter measurements of

HEMT ID	ν_1 (GHz)	$\Delta\nu$ (GHz)
NRAO A-12	31.9	6.05
NRAO A-23	31.5	6.62
MAO-5	31.9 ± 0.3	6.6 ± 0.6

Table 4: Bandpass characteristics of the 5.5-meter receiver with the three HEMTs used in observations.

our calibrator sources (relative to Cas A) onto a 32.0 GHz value using our narrow-band measurement of S_{cas} at this frequency and spectral information culled from the literature, or, for the case of Cas A, obtained from measurements at OVRO. For 3C48, 3C147 and 3C286 we compute effective spectral indices over the 5.5-meter bandpass from the spectral fitting formulae given by (Kellermann et al. 1969), with a standard power law of the form

$$S(\nu) = S(\nu_o) \times \left(\frac{\nu}{\nu_o}\right)^\alpha. \quad (16)$$

Our effective spectral indices for these sources are shown in Table 5. Although the formal errors in these spectral indices given the uncertainties quoted in Kellermann’s fitting formulae are of order 0.01, we adopt error bars of 0.1 in order to allow for the extrapolation to 32 GHz and the possibility of secular evolution of the spectra at high frequency. For NGC 7027, a planetary nebula, we assume $\alpha = -0.1 \pm 0.1$; and for the other 3C sources, we assume that $\alpha = -0.8 \pm 0.1$. Kellermann finds from low frequency ($\nu < 15$ GHz) observations of Cas A that the spectrum is well described by a single power law with $\alpha_{cas} = -0.765 \pm 0.005$. Rather than extrapolate this low frequency result to 32 GHz, we use the 14.5 and 31.7 GHz RING5M measurements of Cas A (Leitch et al. 1999) to compute a spectral index which is more representative of the actual spectrum at our frequency. The RING5M measurements result in $S_{cas,14.5} = 313.6 \pm 8.9$ Jy and $S_{cas,31.7} = 164.2 \pm 5.4$ Jy, implying $\alpha_{cas} = -0.827 \pm 0.056$. This result is slightly steeper than the result of Kellermann at lower frequencies, but still consistent with a single power law over the entire range up to 31.7 GHz. These measurements are also in good agreement with the results of recent observations of Cas A with the BIMA array (Wright et al. 1999). In this analysis, Wright et al. have combined BIMA data at 28 and 83 GHz with 1 and 5 GHz VLA maps of Cas A (Koralesky and Rudnick, 1999) to examine spectral index variations of the various “knots” of emission seen in Cas A at high resolution maps. The spectra of these structures are generally well described by power laws with $-0.81 \lesssim \alpha \lesssim -0.77$, up to and including the 83 GHz data. Since a single dish radio telescope is likely to measure slightly different spectral indices due to the dependence of the spectral indices on spatial scale, we take this as merely suggestive, and adopt the value of α_{cas} computed above to interpolate our 5.5-meter measurements onto 32.0 GHz flux densities for all of our sources. We approximate the spectrum of Jupiter across our band using the model of Trafton (1965) as presented in the context of Wrixon et al.’s (1971) measurements. Using this model, and assuming a constant power-law slope across our band, we compute an effective spectral index of 2.24 from 28.5 to 40.0 GHz, which we use in relating our band-averaged fluxes to 32.0 GHz flux densities; we estimate a 1- σ error of 0.1 in this quantity. For the other planets we assume a thermal ($\alpha = 2$) spectrum, with the same uncertainty. This strategy should do a good job of accounting for the effects of the overall shape of the spectrum on the average

Source	Spectral Index
Cas A	-0.827 ± 0.056
NGC 7027	-0.1 ± 0.1
3C48	-1.18 ± 0.1
3C147	-1.21 ± 0.1
3C286	-0.82 ± 0.1
Jupiter	$+2.24 \pm 0.1$
Saturn	$+2.0 \pm 0.1$
Mars	$+2.0 \pm 0.1$

Table 5: Spectral Indices used for the interpolation from wideband flux measurements to 32.0 GHz flux densities. See the text for details on how the indices and uncertainties were estimated.

brightness temperature from 29 to 35 GHz, but may not get the actual 32.0 GHz brightness temperature for sources with very narrow features in the spectrum (like Mars).

It is well known that the flux density of Cas A is slowly decreasing as a function of time. Baars (1977) gives an expression for the fractional annual decrease in Cas A’s flux density:

$$\frac{\delta S}{S} = [(0.0097 \pm 0.0004) - (0.0030 \pm 0.0004) \log \nu_{\text{GHz}}] \text{yr}^{-1}; \quad (17)$$

where Δt is the time interval in years. $S_{cas,t}$ is then

$$S_{cas,t} = S_{cas,t_0} \times \left(1 - \frac{\delta S}{S}\right)^{\Delta t}. \quad (18)$$

At $\nu = 32$ GHz, this yields a $(0.52 \pm 0.07)\%$ decrease in S_{cas} per year. This functional form for the secular variation has found some support at 15 GHz in the work of O’Sullivan and Green (1999). We take $\frac{\delta S}{S} = 0.52 \pm 0.15 \text{yr}^{-1}$. Using this expression we can compare observations taken at differing epochs to our absolute measurement of Cas A (epoch May 1998). For the epochs we are examining this is at most a 2% correction. A misestimation of the variability of Cas A will increase the variance of the flux ratios we observe for a given source, and hence be automatically accounted for in the final error budget of each source.

For these observations, scans on these calibrators were interleaved with observations of Cas A over a wide range of Hour Angles, allowing an accurate determination of the atmospheric opacity and frequent relative calibration using Cas A. Table 6 shows the average observed flux ratios of our sources for all epochs. Where the epoch-to-epoch scatter in the observed ratios exceeds the mean error bar for a given source, the epoch-to-epoch scatter is adopted as the error in the ratio. This strategy automatically incorporates into our final error bar any systematic errors which may not be manifest in the errors estimated for a given epoch’s observations, such as source variability and any errors in the

characterization of Cas A’s secular behavior. For each source “X” with spectral index α_x , measured relative to a calibrator “C” (with associated flux density $S_{c,32}$ and spectral index α_c) with a rectangular bandpass $\delta\nu$ centered at a frequency ν_1 , the narrow-band flux ratio referenced to an epoch t_o , $R_{32.0,t_o}$, can be shown to be

$$R_{x,32.0,t_o} = R_{x,obs,t} \times \left(1 - \frac{\delta S}{S}\right)^{(-\Delta t)} \times \frac{\alpha_x + 1}{\alpha_c + 1} \times \frac{\nu \left(\frac{\nu}{32}\right)^{\alpha_c} \Big|_{\nu_1 - \delta\nu/2}^{\nu_1 + \delta\nu/2}}{\nu \left(\frac{\nu}{32}\right)^{\alpha_x} \Big|_{\nu_1 - \delta\nu/2}^{\nu_1 + \delta\nu/2}}, \quad (19)$$

where the values of Δt , ν_1 and $\delta\nu$ used are those appropriate to the epoch of observation. These are the ratios we quote in Table 6. While the data have been corrected for atmospheric attenuation using a mean optical depth $\tau = 0.049$, these corrections are relatively unimportant for our measurements since any errors in τ will tend to cancel in the ratio. The flux ratios quoted have also been corrected for the form factor indicated above, and the error bars include a 1.7% systematic error due to the determination of this form factor. Planetary fluxes have been expressed in K/Jy using the relation

$$\frac{T}{S_{cas}} = \frac{\lambda^2 R}{2k \delta\Omega}, \quad (20)$$

where T is the brightness temperature of the planet, $\delta\Omega$ is the solid angle of the planet at the time of the observation (determined from standard ephemerides), R is the observed ratio of the planetary flux to the flux of Cas A, and k is Boltzmann’s constant. For this calculation, we used the value of λ appropriate to each epoch of observation.

With these flux ratios in hand, it is then straightforward to obtain the flux density at 32.0 GHz $S_{x,32}$ of the source “X” :

$$S_{x,32} = R_{x,32,t_o} \times S_{c,32,t_o}. \quad (21)$$

For the case at hand, $S_{c,32,t_o} = 194 \pm 5$ Jy. These results are also shown in Table 6.

Since in general a Gaussian distribution of spectral indices does not give rise to a Gaussian distribution of flux densities, Equations 19 and 21 were jointly evaluated 10^6 times for each source “X” with independently varying R , α_c , α_x , $S_{c,32}$, ν_1 and $\delta\nu$ values drawn from the (assumed Gaussian) populations implied by the error estimates we have quoted above. For R , we have used *each epoch’s* observed flux ratio together with the error bar inferred from the scatter internal to those data. For sources not bright enough to point on, we also included the effects of the residuals in the 5.5-meter pointing model (0.45 rms – an average over all epochs). The error bars quoted in Table 6 are the 68% confidence intervals inferred from this simulation. For the 3C sources and NGC7027, the error intervals inferred are virtually unchanged relative to those which are obtained by ignoring finite

bandpass effects. This is due to the fact that these sources have spectral indices very similar to that of Cas A.

Figure 4 shows the *relative* flux ratio for the five most-observed sources in our sample as a function of epoch. While there is some indication that epochs 4 and 5 may be slightly lower than other epochs, it is difficult to disentangle this effect from the intrinsically large scatter of the data. In particular Jupiter, the brightest of these five sources, shows no departure from the mean greater than 2% in four epochs of observation; NGC7027, the second brightest, shows less than this. The data points for these two brightest sources are shown connected by bold lines in the figure; they are consistent with a constant value of 1.0. For Jupiter, the uncertainties in the source spectra and band characterization have been included in each epoch’s error bar; these uncertainties dominate the uncertainty in the epoch 5 flux ratio.

Some of these sources are at least slightly variable, and the variability of some of them is not known. Based on our observations and existing data, we designate the planets, plus NGC7027, 3C48, 3C147, and 3C286 as useful calibrators at 32.0 GHz. There are indications that 3C147 may be slightly variable. For convenience, we summarize our findings for these sources in Table 7. Our brightness temperature for Mars has been corrected from a mean heliocentric radius of 1.658 AU for the epochs of observation to a fiducial heliocentric radius of 1.524 AU using an $r^{0.25}$ law (Epstein, 1971) to facilitate comparison with other measurements. In this table we have adopted the more precise Leitch (1998) values for S_{3c286}/S_{cas} and T_{Jup}/S_{cas} .

Source	Epochs	Mean Flux Ratio	$S_\nu(32)$ or $T(32)$
NGC7027	1-3	$(2.76 \pm 0.02) \times 10^{-2}$	5.50 ± 0.20 Jy
3C48	2,5	$(4.37 \pm 0.40) \times 10^{-3}$	0.86 ± 0.08 Jy
3C84	4,5	$(6.22 \pm 0.03) \times 10^{-2}$	12.3 ± 0.4 Jy
3C147	1-5	$(7.29 \pm 0.28) \times 10^{-3}$	1.44 ± 0.08 Jy
3C218	2,3	$(9.55 \pm 0.28) \times 10^{-3}$	1.88 ± 0.06 Jy
3C273	4,5	$(2.14 \pm 0.02) \times 10^{-2}$	42.4 ± 1.6 Jy
3C286	2-5	$(9.83 \pm 0.42) \times 10^{-3}$	1.95 ± 0.11 Jy
3C345	5	$(5.10 \pm 0.11) \times 10^{-2}$	10.11 ± 0.43 Jy
3C353	2,3	$(1.92 \pm 0.02) \times 10^{-2}$	3.80 ± 0.43 Jy
Jupiter	2-5	0.800 ± 0.030	$155.1_{-5.7}^{+6.8}$ K
Mars	2,3	0.990 ± 0.028	$196.0_{-7.6}^{+7.5}$ K
Saturn	4,5	0.726 ± 0.019	$140.8_{-4.9}^{+4.4}$ K

Table 6: Observed ratios of calibrator sources relative to Cas A. Planets’ relative fluxes are expressed in units of K/Jy. All fluxes have been corrected to epoch May 1998 on an epoch-by-epoch basis, and interpolated onto narrowband flux ratios using Equation 19.

Source	S_ν (Jy) or T (K)
Cas A ^A	(194 ± 5) Jy
NGC7027	5.45 ± 0.20 Jy
3C48	0.86 ± 0.08 Jy
3C147	1.44 ± 0.08 Jy
3C286	$2.02_{-0.06}^{+0.05}$ Jy
Jupiter	152 ± 5 K
Saturn	141_{-5}^{+4} K
Mars ^B	200 ± 8 K

^A 32.0 GHz flux density standard.

^B T_{Mars} corrected to 1.524 AU heliocentric radius; see text for details.

Table 7: 32.0 GHz Calibrator Flux Densities and Brightness Temperatures

7. Discussion and Conclusion

We have presented an accurate measurement of the 32 GHz flux density of Cas A, $S_{cas,1998} = 194 \pm 5$ Jy . This is the first direct measurement of S_{cas} above 16 GHz. This measurement provides a firm foundation for calibrating experiments in the vicinity of 32 GHz. The resulting flux scale has an uncertainty of 2.5%, a significant improvement over other flux density scales at this frequency, most of which contain uncertainties $> 6\%$.

By way of comparison, the RING5M program conducted at OVRO recently derived S_{cas} relative to observations of DR21 on the OVRO 5.5-m telescope at 32 GHz (Leitch et al., 1999). Using Dent’s (1972) flux density for DR21, and applying the form factor for the OVRO 5.5-m beam derived from a 32 GHz map of Cas A made with the Effelsburg telescope (see § 6) , they find $S_{cas,1996} = 195.8_{-5.7}^{+6.4}$ Jy, corresponding to $S_{cas,1998} = 193.8_{-5.7}^{+6.4}$ Jy. This is in agreement with the result reported in this paper.

Until the RING5M calibration work, the OVRO Ka-band flux density scale was based on the Wrixon et al.(1971) absolute measurement of Jupiter, $T_J = 144 \pm 8$ K. This implies $S_{cas,1996} = 185.5 \pm 10.3$ Jy, consistent with both this absolute measurement and the analysis relative to DR21 (although the latter is not completely independent of it), but with an associated error of 5.5%, more than twice that in our measurement of Cas A. The Kellermann scale implies $S_{cas,1994} = 186.5 \pm 3.7$, including only formal errors in the Kellermann scale, but with a much larger error associated with the extrapolation to 32 GHz and the secular correction. The Saskatoon experiment (Netterfield, 1997) estimated an uncertainty of 13% in this value.

We have also presented absolute flux densities for a standard set of centimeter-wavelength calibrator sources, including Jupiter and Mars. These measurements should facilitate the calibration of experiments at a wide range of angular scales and terrestrial latitudes. These measurements have $1 - \sigma$ accuracies ranging from 3% (for Jupiter) to 9% (for 3C48). Our measurement for 3C286 is also in good agreement with that of Leitch (1998), who finds $S_{3C286}(32 \text{ GHz}) = 2.02 \pm 0.07$. Our inferred brightness temperature for Jupiter ($T_J = 152 \pm 5$ K) is in excellent agreement with both Wrixon’s $T_J = 144 \pm 8$ K, and the RING5M (Leitch et al., 1999) value of 152 ± 5 K. We emphasize that the Leitch value of T_J is independent of our quoted value insofar as the absolute calibrations of these experiments were independent. Our measurement of $T_{Mars} = 200 \pm 8$ K is consistent with the results of Hobbs and Knapp (1971), who find $T_{Mars} = 207 \pm 13$ K at 9.55 mm, and with Ulich (1981) who finds $T_{Mars} = 194 \pm 8.2$ K at 9.5 mm. All of these results are referred to a standard solar distance of 1.524 AU. The compilations of microwave observations of Mars given by Epstein (1971) and Efanov et al. (1971) are also in good agreement with our measurement near 1 cm; our results are significantly more precise than any of the 1-cm

measurements reported in these compilations. Our measurements of these sources offer an excellent basis for the calibration of current and future experiments in the vicinity of 32 GHz.

This work would not have been possible without the expertise of the OVRO staff; in particular, we acknowledge the assistance of Russ Keeney for his work on both the 1.5-meter and 5.5-meter telescopes, and Stan Hudson for constructing the cold load box. We thank the OVRO Millimeter Array staff for useful discussions and periodically loaning us equipment, and Ken Kellermann, Tim Pearson, and Ed Wollack for comments on the manuscript which improved the content and presentation. We acknowledge NRAO, Princeton University, and the MAP collaboration for loaning us the HEMT used in the October 1998 5.5-meter observations. For part of the duration of this work, BSM was supported by the Zacheus Daniels fund at the University of Pennsylvania. STM was supported by an Alfred R. Sloan Fellowship at the University of Pennsylvania. The work was supported in part by NSF grant AST-9419279.

REFERENCES

- Baars, J.W.M., Genzel, R., Pauliny-Toth, I.I.K., and Witzel, A. 1977, *Astron. Astrophys.*, 61, 99-106.
- Baird, Ramon C., Newell, Allen C., and Stubenrauch, Carl F. 1988, *IEEE Transactions on Antennas and Propagation*, v.36 no.6, 727.
- Berge G.L. & Gulkis, S. 1976, in *Jupiter*, T. Gehrels, Ed. (Univ. of Arizona Press, Tucson), 621-692.
- Dent, William A. 1972, *Ap.J.* , 177, 93.
- Devlin M.J., De Oliveira-Costa A., Herbig T., Miller A.D., Netterfield C.B., Page L.A., Tegmark M., 1998, *Ap.J.Lett.*, 509, L69.
- Efanov, V.A., Moiseev, I.G., Kislayakov, A.G. and Naumov, A.I. , *Icarus*, 14,198.
- Epstein, Eugene E. 1971, *Icarus*, 14,214.
- Francis, Michael H., private communication, 1998.
- Francis, M. H., Kremer, D.P., and Repjar, A.G. 1990, *Microwaves & RF*, March 1990, 77.
- Hemmati, Hamid, Mather, John C., and Eichorn, William L. 1985, *Applied Optics*, 24 , 4489.
- Herbig, T. 1994, Ph.D. thesis, Caltech.

- Hobbs, R.W. and Knapp, S.L. 1971, *Icarus*, 14, 204.
- Jones, Michael E., Scott, P.F., 1998, *Proceedings of the 33rd Rencontres de Moriond*.
- Kellermann, K.I., 1964, *A.J.* , 69,205.
- Kellermann, K.I., Pauliny-Toth, I.I.K., and Williams, P.J.S. 1969, *Ap.J.*, 157, 1.
- Koralesky, B., and Rudnick, L. 1999, *ApJ* (in press).
- Krauss, J.D. 1986, *Radio Astronomy* (Ohio: Cygnus-Quasar Books).
- Leitch, E.M. 1998, PhD. Dissertation, Caltech.
- Leitch, E.M., Readhead, A.C.S., Pearson, T.J., Myers, S.T., and Gulkis, S. 1999, to appear in *ApJ*, 518.
- Lemanczyk, Jerzy, and Larsen, F. Holm 1988, *IEEE Transactions on Antennas and Propagation*, 36, 845.
- Lo, Y.T., & Lee, S.W.,eds., 1993, *Antenna Handbook v.IV* (New York: Van Nostrand Reinhold).
- Miller A.D., Caldwell R., Herbig T., Page L., Torbet E., Tran H., Devlin M., Puchalla J., 1999, *Ap.J.*, submitted.
- Myers, S.T., Baker, J.E., Readhead, A.C.S., Leitch, E.M., and Herbig, T. 1997, *Ap.J.*, 485,1.
- Netterfield, C.B., Devlin, M.J., Jarosik, N., Page, L., and Wollack, E. 1997, *A.J.*, 474, 47-66.
- Newell , A.C., Ward, R.D., and McFarlane, E.J. 1988, *IEEE Transactions on Antennas and Propagation*, 36, 792.
- National Institute of Standards and Technology 1990, “NIST Report of Special Test on 1.5-m Offset Cassegrain Clear Aperture Antenna at 32 GHz”, May 1990.
- O’Sullivan, C., and Green, D.A. 1999, *MNRAS* , 303, 573-578.
- Rahmat-Samii, Y. “Modern Concepts in Analysis, Synthesis and Measurements of Antennas” in *Modern Radio Science 1993*, ed. H. Matsumoto.
- Readhead, A.C.S., Lawrence, C.R., Myers, S.T., Sargent, W.L.W., Hardebeck, H.E., and Moffet, A.T. 1989, *Ap.J.*, 346,566.
- Readhead, A.C.S., Padin, S., Pearson, T.J., Cartwright, J., and Myers, Steven T., in preparation; also <http://astro.caltech.edu/~tjp/CBI/>.
- Scott, P.F., Saunders, Richard, Pooley, Guy, O’Sullivan, Creidhe, Lasenby, A.N., Jones, Michael, Hobson, M.P., Duffett-Smith, P.J., Baker, Joanne 1996, *Ap.J.Lett.*, 461, L1.
- Rohlfs, K. and Wilson, T.L. 1996, *Tools of Radio Astronomy* (Berlin: Springer-Verlag).

- Torbet E., Devlin M.J., Dorwart W.B., Herbig T., Miller A.D., Nolte M.R., Page L., Puchalla J., Tran H.T., Ap.J., in press.
- Trafton, L.M. 1965, Ph.D. thesis, California Institute of Technology.
- Ulich, B.L. 1981, AJ, 86,11.
- Wang, Johnson J.H. 1988, IEEE Transactions on Antennas and Propagation, 36 , 746.
- White, Martin, Carlstrom, John E., and Dragovan, Mark, Ap.J., submitted.
- Wright, M., Dickel, J., Koralesky, B., and Rudnick, L. 1999, astro-ph/9901417.
- Wrixon, G.T., Welch, W.J., and Thornton, D.D. 1971, Ap.J. , 169,171.

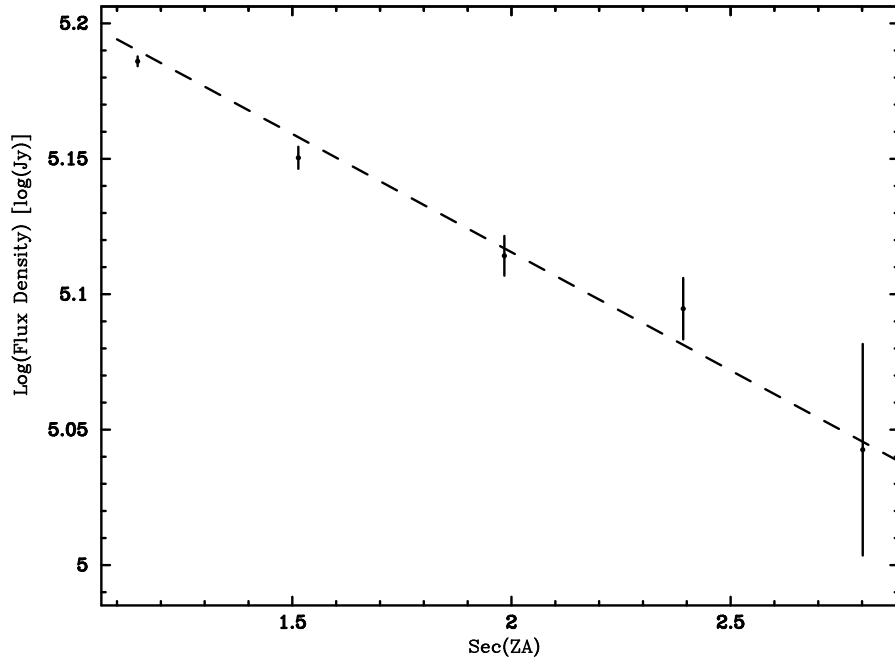


Fig. 1.— 10 May 1998 - 16 May 1998 FLUX observations of Cas A, uncalibrated for atmospheric attenuation. The best straight-line fit of the natural log of the source flux density to $\sec(ZA)$ is shown as a dashed line; this line corresponds to $\tau = 0.071$. The increased error bars at high airmass are due the smaller number of data per bin, in addition to the $\sim 1.6\%$ gradient in the FLUX as a function of parallactic angle discussed in the text.

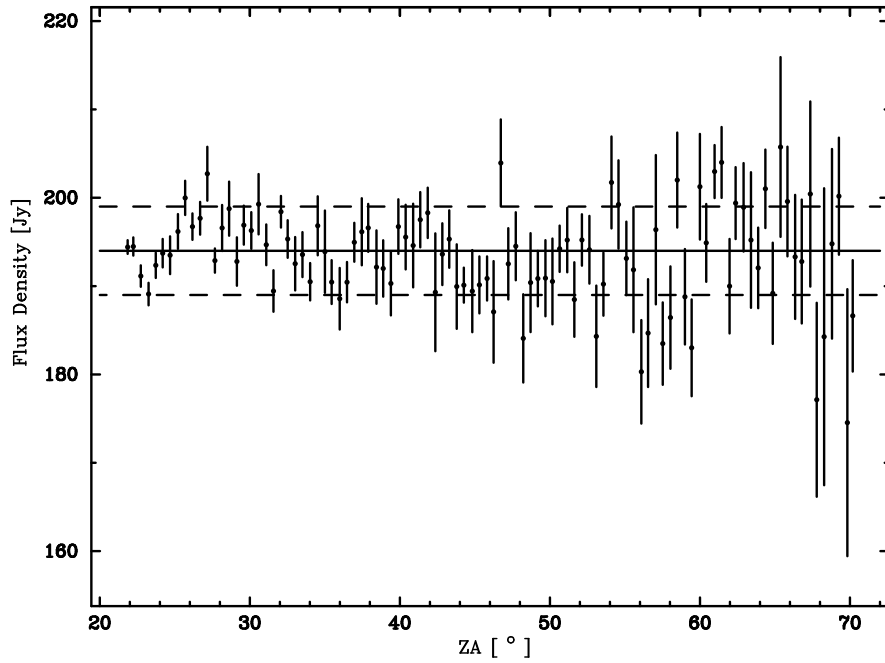


Fig. 2.— 10 May 1998 - 16 May 1998 FLUX observations of Cas A versus zenith angle, calibrated for atmospheric attenuation. The feature at $ZA \sim 28$ is most likely residual ground spillover (~ 1.5 mK). The solid line is the average of all FLUXes; the dashed lines indicate the range of values included at the 68% confidence level using our estimated systematic errors ($S_{cas} = 194 \pm 5$ Jy).

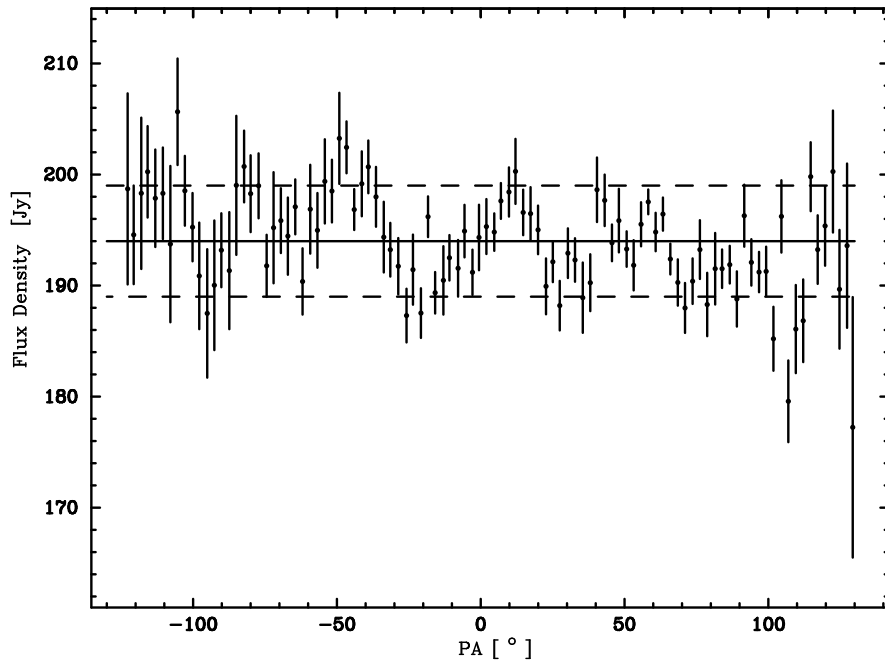


Fig. 3.— 10 May 1998 - 16 May 1998 FLUX observations of Cas A versus parallactic angle, calibrated for atmospheric attenuation. The slight overall gradient is due to an ambient temperature effect discussed in the text.

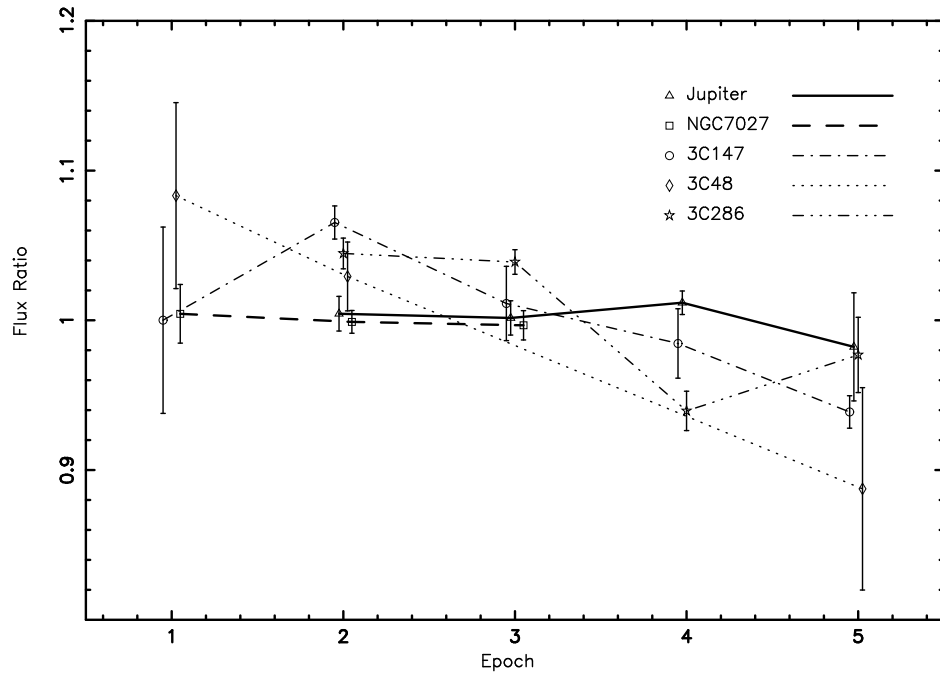


Fig. 4.— Flux ratios for the best potential calibrator sources in our sample relative to Cas A. The flux ratio for each epoch of each source has been divided by the mean flux ratio for that source; Jupiter has been corrected for the bandpass characteristics quoted in Table 4. All sources been corrected for the secular evolution of Cas A.